

Cluster STEP

J. Young^{1*} and Other.

¹*OSU/USM*

2013

ABSTRACT

Shape measurement bias is an important source of error in the mass of clusters as determined by weak gravitational lensing. The cluster mass function as measured by weak lensing for the Dark Energy Survey (DES) will be used to constrain cosmology, so it is important that shape measurement bias is small. Comparing the current level of systematic bias of different weak lensing pipelines measured on simulated images allows us to model the expected error in the cluster mass measurement for the stacked weak lensing result. The accuracy of the shape measurement pipelines is determined from image simulations that have the expected distribution of galaxy properties that will be observed by DES. Eight different shape measurement pipelines, including several which have not competed in previous image simulation challenges are included. The best performing weak lensing pipelines exhibit a multiplicative bias of several percent, that is stable as a function of redshift. This level of shape measurement bias does not have a statistically significant impact on DES cluster cosmology.

Key words: gravitational lensing; weak, techniques:image processing

1 INTRODUCTION

The abundances and masses of galaxy clusters provide an important constraint on cosmology (Weinberg et al. 2012). Weak lensing is the most direct way to measure cluster masses for large optical surveys such as the Dark Energy Survey (DES) (<http://www.darkenergysurvey.org/>), which due to the depth and size observed will very accurately measure the halo mass function. Measuring the correlated distortion in the shape of galaxies caused by lensing is complicated by the distortion of observed images caused by the atmosphere and telescope optics, called the Point Spread Function or PSF. Shape measurement pipelines have been developed to remove the distortion caused by the PSF and accurately measure the lensing signal. Previous studies have shown the importance of calibrating shape measurement pipelines for a weak lensing measurement of cluster mass (Applegate et al. 2012). The mass of clusters measured by four different groups were systematically biased, which the authors concluded was probably dominantly due to shape measurement bias.

Previous image simulation challenges were used to determine the accuracy of shape measurement pipelines. Four publicly available weak lensing challenges STEP1 (Heymans et al. 2006), STEP2 (Massey et al. 2007), GREAT08 (Bridle et al. 2010), GREAT10 (Kitting et al. 2012) used blinded

image simulations to characterize the shape measurement bias created by different lensing pipelines. Results from these challenges have been used to calibrate shape measurement pipelines (Applegate et al. 2012), determine that lensing pipelines meet accuracy requirements for scientific analysis (Bergé et al. 2008), and provide insight for further pipeline development. These previous challenges focused on calibrating shear measurement pipelines in the cosmic shear regime ($|\gamma| < 0.6$) and on the importance of shape measurement bias for the shear power spectrum of large scale structure. These image simulations were created to study how specific galaxy and PSF properties affected the accuracy of shape measurements, rather than on the total shape measurement bias expected for any specific optical survey.

To determine the error on the cluster mass measurement in a specific survey due to shape measurement bias it is important to use image simulations that have similar properties to the data. The size, shape, morphology, and signal-to-noise ratio of sources all impact the accuracy of the lensing pipelines, as does the strength of the lensing signal. For the cluster shear regime both the quadratic (Q) and multiplicative (M) shape measurement bias affect the lensing signal, and it is important to quantify these on images with simulated shear comparable to the shear observed around large galaxy clusters. For an accurate characterization of the level of shear measurement bias, it is important to test the current implementation of lensing algorithms. There are several new implementations of lensing pipelines being tested for implementation in DES that are included

* E-mail: email@address (AVR); otheremail@otheraddress (ANO)

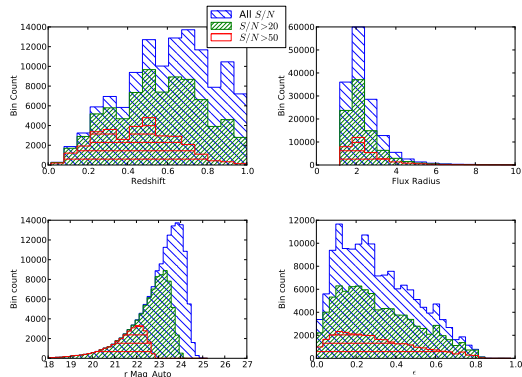


Figure 1. This figure shows distributions of various galaxy properties in the CSTEP simulation. The top left corner shows the distribution in redshift, the top right corner shows the distribution in size (flux radius in pixels), the bottom left corner shows the distribution in magnitude, and the bottom right corner shows the distribution in intrinsic ellipticity.

in this project, which have not been run in previous image simulation challenges.

The Cluster SHeAr TESting Program (CSTEP) tested eight weak lensing pipelines on images of constant shear ($|\gamma| = [0.03, 0.06, 0.09, 0.15]$) with galaxy and PSF properties that simulate the properties of data that will be observed with DES. Shape measurement errors were quantified by the Q, M and C determined by

$$\gamma_m = Q(\gamma_t)^2 + M(\gamma_t) + C \quad (1)$$

where γ_t is the true shear and γ_m is the measured shear. Lensing pipelines were evaluated to determine if their shape measurement bias was constant as a function of simulated redshift which is important to the accuracy of the halo mass function. The bias as a function of redshift determined for the lensing pipelines was used to model the expected error in the cluster mass from shape measurement bias. In each mass and redshift bin expected for the stacked weak lensing analysis of DES, the NFW reduced shear profile of the average halo was transformed by the shear measurement bias. This biased NFW was fit to determine what halo mass would be measured from this biased shear profile. The true and biased mass were compared to determine the percentage error on the mass, due to shape measurement bias.

In this paper section 1 details the image simulations used in this project, section 2

2 SIMULATIONS

The image simulations used in the CSTEP project were designed to replicate the quality of the final co-added data that will be taken by the Dark Energy Survey. The Dark Energy survey is an optical survey of 5000 deg² of the southern sky,

that will image around 300 million galaxies in five filters (g,r,i,z and Y) (Honscheid & DePoy 2008). To test the DES data management system and software pipelines developed by the science working groups detailed image simulations were created by the DES Simulation team. The software used to simulate these images was created by Huan Lin, N. Kuropatkin and C. Stoughton, and is described in (Mohr et al. 2008). Each simulated image used in CSTEP models the DES focal plane with 62 2K by 4K pixel (0.27"/pixel) CCD chips. Star and galaxy objects are rendered by calculating the intensity of each pixel by drawing random samples of photons from the theoretical light profile of the source convolved by the PSF.

For the CSTEP simulated images mock galaxy catalogs were created with the ADDGALS method that reproduced observed correlations for galaxies among clustering, luminosities, and colors. The parent N-body simulations used by ADDGALS are the “Carmen” Las Damas N-body simulation box (1 Gpc/h) with flat Λ CDM, $\Omega_M = 0.25$, $\Omega_\Lambda = 0.75$, $\sigma_8 = 0.8$, $z < 1.35$ (McBride et al. (2009)). In each image around 140,000 galaxy objects are present. The simulated galaxy images are designed to have similar properties to the galaxies that the DES survey will observe by combining a mock catalog with empirical data from the HST/GEMS catalog for galaxies with magnitude $r > 23$, and from the SDSS stripe 82 coadded image for galaxies with magnitude $r < 23$. The distributions of various galaxy properties in the simulation are shown in Figure 1. The galaxy objects are created with Sersic profiles with an index that ranges from 0.5 to 5.

The CSTEP simulated images contain a constant PSF which separates the technical challenge of how to best model a varying PSF from that of determining the best lensing pipeline. For CSTEP there are two branches in the image simulation sets, those that include a circular Gaussian PSF and those that include an elliptical Gaussian PSF. The elliptical Gaussian PSF has $\epsilon = 0.03$. For both the Gaussian and elliptical Gaussian PSF the simulated images contain a convolution kernel that mimics the range of isotropic distortion due to the atmosphere that DES will likely observe. This isotropic distortion simulates seeing conditions, or atmospheric blurring, of 0.7 – 0.9 arcsec. A summary of the PSF image properties is included in Table 1. For each PSF there are 8 focal plane images that contain constant shear for $\gamma = 0.0$ to $\gamma = 0.15$ in two components (γ_1 and γ_2) as described in Table 1.

3 SHAPE MEASUREMENT PIPELINES

There are eight weak lensing pipelines that submitted results for the CSTEP project and are shown in Table 2. The lensing pipelines tested are implementations that potentially will be used to create shear catalogs for DES. These implementations represent a broad range of lensing pipeline types, and can be divided into four groups. Methods are grouped using roughly the same criteria as in STEP2 (Massey et al. 2007). A short description of the methods is included below with a detailed pipeline description included in Appendix A.

PSF Number	Type	Seeing
1	circular Gaussian	0.7
2	circular Gaussian	0.8
3	circular Gaussian	0.9
4	elliptical Gaussian	0.75
5	elliptical Gaussian	0.8
6	elliptical Gaussian	0.9

Shear Number	γ_1	γ_2
1	0.0	0.03
2	0.0	0.06
3	0.0	0.09
4	0.0	0.15
5	0.03	0.0
6	0.06	0.0
7	0.09	0.0
8	0.15	0.0

Table 1. A summary of the PSF and shear sets for the CSTEP simulated images.

3.1 Red class methods

The red class methods (DE, IM, PK, KM) are based on the oldest shape measurement method KSB+ developed by (Kaiser, Squires & Broadhurst 1995). As in STEP2 red class methods are defined as those that measure combinations of moments of each galaxy image $I(x)$ using a Gaussian weighting function of size r_g . Various implementations of this class of methods has been studied in previous shape measurement challenges, and the accuracy has been shown to vary widely (Massey et al. 2007; Kitching et al. 2012). Two of the lensing pipeline implementations included in CSTEP have performed well on previous image simulations challenges (DE, KM), and other red class implementations that have been shown to be accurate on simulated image data have been used in several recent weak lensing analysis including (Aplegate et al. 2012; Schrabback et al. 2010). Many of the large weak lensing cluster studies have used red class methods (Mahdavi et al. 2013) and it is one of the more commonly used algorithms.

3.2 Green class methods

The green class methods (GM, I3) are the methods which are commonly known as model fitting methods. These methods convolve various models of galaxies with different parameterizations include intrinsic shape, with the PSF and determine those that best fit the galaxy image. Green class methods *lensfit* and DeepZot were among the best performing methods in GREAT08 and GREAT10, and im3shape has been shown to perform well on the GREAT08 and GREAT10 data (Zuntz et al. 2013). A green class method *lensfit*, was determined to be the lensing pipeline capable of producing the best weak lensing catalog of the data of Canada-France-Hawaii Telescope Lensing Survey (CFHTLenS) (Heymans et al. 2012). This catalog was then used for several scientific analysis including (Heymans et al. 2013; Gillis et al. 2013; Kilbinger et al. 2013).

Contributor	Key	Method	Class
P. Melchior	DE	DEIMOS	Red
E. Sheldon	GM	Gaussian Mixtures	Green
B. Rowe	I3	im3shape	Green
J. Young	IM	IMCAT	Red
P. Melchior	KM	ksbm	Red
M. Jarvis	MJ	Bernstein and Jarvis (2002)	Blue
D. Gruen	PK	PKSB	Red
D. Gruen	PF	PFDNT	Purple

Table 2. A summary of the lensing pipelines used to analyze CSTEP simulated images.

3.3 Blue class methods

The blue class methods (MJ) are methods which model the galaxy images as a sum of orthonormal Gauss-Lagurre polynomial functions, commonly known as *shapelet* methods. The MJ method uses an elliptical version of these shapelet basis functions, while other methods use a circular version. The MJ method finds a coordinate system in which the galaxy model is round. The round model is then convolved with the PSF and compared to the galaxy image. The MJ method competed in the STEP1, STEP2, and GREAT08 challenge, and is currently incorporated into the DES data management system. Recently the first example of a blue class method used to analyze survey data compared joint weak lensing and X-ray analysis of 4 deg^2 from the CFHTLS and XMM-LSS surveys of galaxy clusters (Bergé et al. 2008).

3.4 Purple class methods

The purple class method PFDNT incorporates several recent developments in shape measurement. A new shape measurement algorithm, Fourier Domain Null Testing (FDNT) (Bernstein 2010), was recently proposed. To measure the shape of galaxies, both the observed galaxy $I(x)$ and the PSF are transformed into Fourier domain. The shear is measured by determining which γ_1 and γ_2 pass a series of null tests. A FDNT pipeline was able to perform with incredible accuracy on new blinded GREAT08 low-noise images achieving a Q value of 2997. The PFDNT implementation uses another proposed method to improve shape measurement accuracy, that of combining information from multiple lensing pipelines. The shape measurement information of the PKSB pipeline was incorporated into a FDNT pipeline for the PFDNT implementation tested in CSTEP.

4 SHAPE MEASUREMENT BIAS

In this section we summarise the shape measurement bias of the lensing pipelines as measured on the CSTEP simulations. The shape measurement bias is determined for a representative DES lensing, as a function of signal to noise ratio, as a function of redshift. A more detailed examination of the performance of each individual lensing

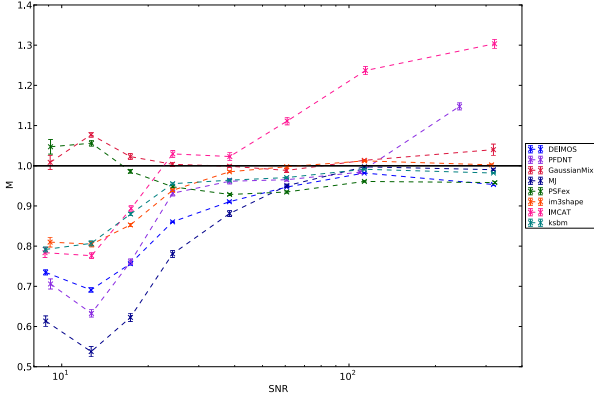


Figure 2. This figure shows the behavior of the shape measurement pipelines as a function of Signal to Noise Ratio.

pipeline as a function of PSF ellipticity. PSF size, galaxy size, and selection bias is included in Appendix A.

4.1 Galaxy signal to noise ratio

The level of pixel noise present on galaxy images greatly impacts the ability of lensing pipelines to accurately measure shear. The impact of pixel noise on shape measurements has been studied in (Melchior & Viola 2012; Okura & Futamase 2013; Refregier et al. 2012) and varies depending on both the source galaxy population and the lensing pipeline. There have been a number of calibration schemes that attempt to correct for the affect of noise bias for specific lensing pipelines developed including (Kacprzak et al. 2012) and (Miller et al. 2013) on previous image simulations. The noise bias of lensing pipelines as measured on the CSTEP image simulations may improve with further pipeline development as new methods of noise bias correction are implemented.

The signal to noise level (S/N) was measured on the CSTEP images for each galaxy object using the SExtractor software package (Bertin & Arnouts 1996) with S/N defined as

$$S/N = \frac{\text{Flux}}{\text{Flux Error}} \quad (2)$$

and where the flux was determined using automatic aperture magnitudes. To make the results easier to interpret and compare to previous studies the bias of the lensing pipelines was quantified in this section by

$$\gamma_m = M(\gamma_t) + C \quad (3)$$

where γ_t is the true shear and γ_m is the measured shear. The results of the bias as a function of S/N are shown in Figure 2.

4.2 Average results on galaxies S/N > 20

In this section we include the average shape measurement bias results on a representative DES lensing catalog of all sources S/N > 20. Most previous weak lensing studies rejected all objects below a set S/N threshold, but the depth chosen varies as it is determined by both the capabilities

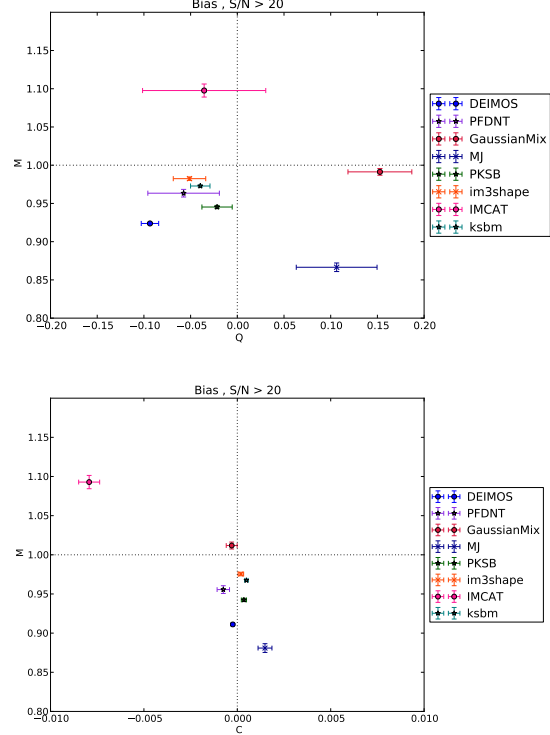


Figure 3. This figure shows the average shape measurement bias as measured on all images for galaxy objects SNR > 20. The top panel shows the shape measurement bias Q,M as measured using a Q,M,C fit. The bottom panel shows the shape measurement bias M,C as measured using a M,C fit.

of the lensing pipeline used and the type of lensing analysis. In the CFHTLenS survey all objects were rejected that were measured as $i'(AB) < 24.7$, or a S/N limit of around 10 (Miller et al. 2013). This limit was imposed for the CFHTLenS catalog as it was the depth determined at which the photometric redshifts and shape measurements were too poorly measured (Hildebrandt et al. 2012). For the CSTEP project we chose objects S/N > 20 for the representative DES lensing catalog. This is a conservative choice, and with additional lensing pipeline development a lower S/N threshold could be chosen for the final DES lensing catalog.

The average shape measurement bias on all images in the CSTEP simulations for galaxies S/N > 20 are shown in Figure 3. Three of the lensing pipelines (I3, DE, KM) that are included in the cluster STEP results, also competed in the GREAT10 challenge. The comparison between the GREAT10 and CSTEP results is shown in Figure 4. The results are roughly consistent between the two challenges for I3 and KM showing that both pipelines are robust, and demonstrate similar levels of shape measurement bias for a wide variety of sources and PSF types. Both I3 and KM are among the best performing lensing pipelines for both CSTEP and GREAT10.

4.3 Selection effects and pipeline efficiency

When running on images lensing pipelines are not able to return a successful shear measurement for all objects. If lens-

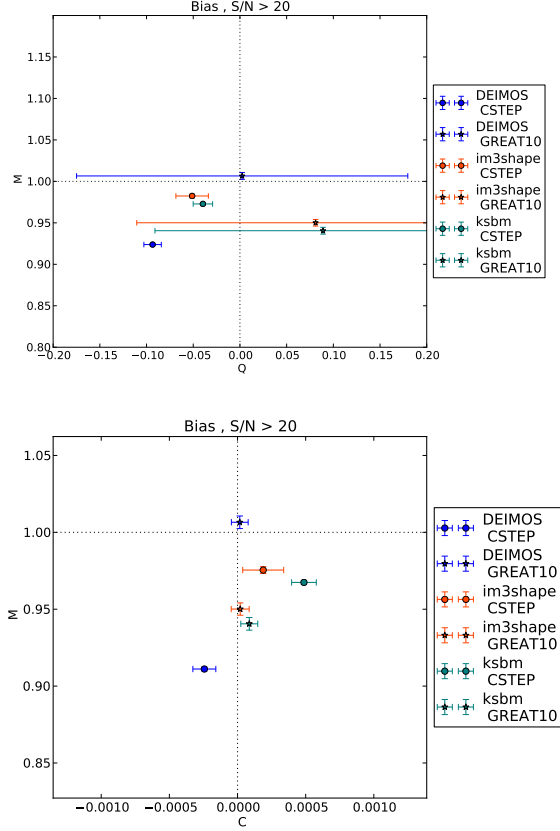


Figure 4. This figure shows the average shape measurement bias as measured on all images for galaxy objects SNR > 20 on CSTEP data and the shape measurement bias as measured by the same lensing pipelines on the GREAT10 data (Kitching et al. 2012). The top panel shows the shape measurement bias Q, M as measured using a Q, M, C fit. The bottom panel shows the shape measurement bias M, C as measured using a M, C fit.

ing pipelines selectively reject more elliptical objects this can lead to an effect known as selection bias, since $\langle \epsilon \rangle \neq 0$. This effect has been discussed in STEP1 where it was determined that results for some lensing pipelines improved when the non-zero mean ellipticity of the surviving objects was corrected for.

A table of the surviving number of galaxies for each pipeline is included below for sources for sources SNR > 20 in Table ?? . The pipelines that returned the highest efficiency of successful measurements are PKSB, DEIMOS and ksbm. Gaussian mixtures uses a weighting system therefore the total number of sources that return a shear measurement is not comparable since many of these sources are down-weighted. The results seen in CSTEP are similar to those seen in previous lensing challenges in regards to which class of pipeline type is the most robust. The moment based pipelines DEIMOS, PKSB, ksbm are more robust. With the current quality cuts in place DEIMOS has a higher survival rate, but is less accurate than im3shape.

For lensing applications where the number of background sources are small the two best pipelines are ksbm and PKSB. Both of these pipelines are fairly accurate and return a reasonable number of measured objects.

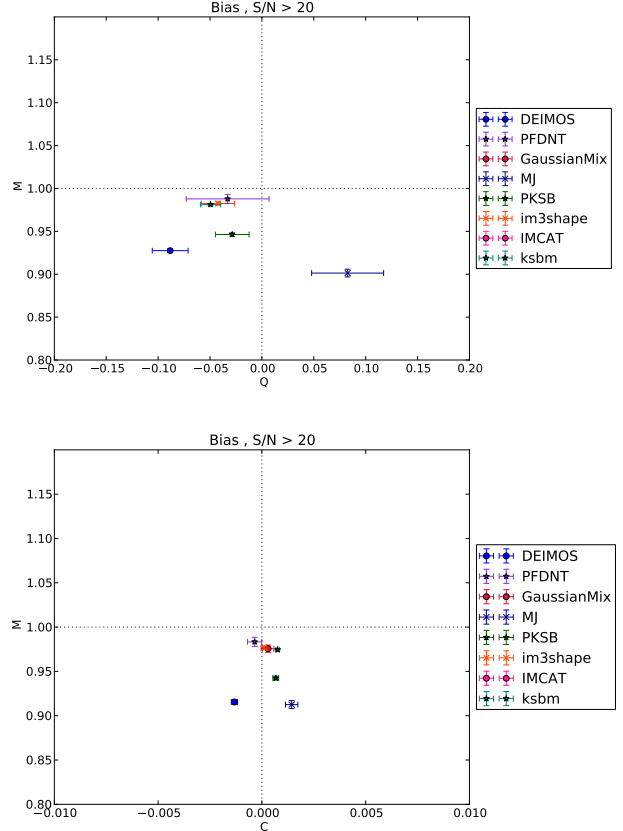


Figure 5. This figure shows the average Q and M results for all pipelines for objects SNR > 20 after correcting for selection effects in the top panel. This figure shows the average M and C results for all pipelines for objects SNR > 20 after correcting for selection effects in the bottom panel.

Pipelines may reject objects in a ellipticity dependent way. To test for this selection effect bias, the γ measured is corrected for the intrinsic ellipticity of the sources as measured by each lensing pipeline. After correcting for selection bias some pipelines, im3shape and DEIMOS have the same level of shape measurement bias. The pipeline that is most effected by selection bias is PFDNT. Q, M and C as measured for each lensing pipeline after correcting for selection effects is included in Table 3 and Table 4 . The average Q, M and C after correcting for selection effects is shown in Figure 7. The distribution of Q, M and C after correcting for selection effects, when measured from each PSF individually is shown in Figure ??.

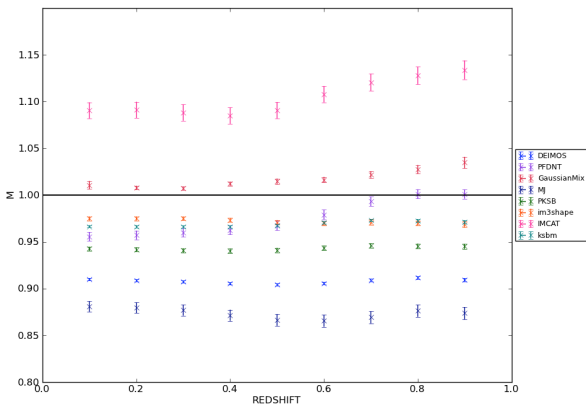
4.4 Shape measurement bias as a function of Redshift

To insure that the cosmology extracted using the halo mass function as measured on galaxy clusters using weak lensing is accurate it is important that galaxy clusters at various redshifts have similar levels of shape measurement bias. The population of galaxies observed at different redshifts will vary in S/N , ellipticity distribution, size and morphology all properties which can effect the accuracy of a lensing measurement. The bias of galaxy sources with $S/N > 20$ as a

Pipeline	Qsel	Msel	Csel	Q	M	C	efficiency
DEIMOS	-0.088 ± 0.017	0.928 ± 0.002	-0.0014 ± 0.0002	-0.094 ± 0.009	0.924 ± 0.001	-0.0004 ± 0.0001	0.886
PFDNT	-0.033 ± 0.040	0.988 ± 0.005	-0.0004 ± 0.0003	-0.058 ± 0.038	0.963 ± 0.005	-0.0008 ± 0.0003	0.798
GaussianMix	0.236 ± 0.032	0.944 ± 0.004	0.0006 ± 0.0003	0.153 ± 0.034	0.991 ± 0.004	-0.0001 ± 0.0003	0.897
MJ	0.083 ± 0.035	0.901 ± 0.004	0.0015 ± 0.0003	0.106 ± 0.043	0.867 ± 0.006	0.0016 ± 0.0004	0.778
PKSB	-0.029 ± 0.016	0.946 ± 0.002	0.0006 ± 0.0001	-0.022 ± 0.016	0.945 ± 0.002	0.0003 ± 0.0001	0.855
im3shape	-0.042 ± 0.016	0.983 ± 0.002	0.0000 ± 0.0001	-0.051 ± 0.017	0.982 ± 0.002	0.0001 ± 0.0002	0.750
IMCAT	-0.020 ± 0.058	1.275 ± 0.008	-0.0066 ± 0.0005	-0.035 ± 0.066	1.098 ± 0.009	-0.0080 ± 0.0006	0.526
ksbm	-0.050 ± 0.010	0.981 ± 0.001	0.0007 ± 0.0001	-0.040 ± 0.010	0.973 ± 0.001	$0.0004 \pm$	0.881

Table 3. The Q, M, C results for objects SNR > 20 after correcting for selection effects.

Pipeline	Msel	Csel	M	C
DEIMOS	0.915 ± 0.002	-0.0013 ± 0.0002	0.911 ± 0.001	-0.0002 ± 0.0001
PFDNT	0.983 ± 0.005	-0.0004 ± 0.0003	0.956 ± 0.005	-0.0007 ± 0.0003
GaussianMix	0.976 ± 0.004	0.0003 ± 0.0003	1.012 ± 0.004	-0.0003 ± 0.0003
MJ	0.913 ± 0.004	0.0014 ± 0.0003	0.881 ± 0.006	0.0015 ± 0.0004
PKSB	0.942 ± 0.002	0.0007 ± 0.0001	0.942 ± 0.002	0.0004 ± 0.0001
im3shape	0.977 ± 0.002	0.0001 ± 0.0001	0.975 ± 0.002	0.0002 ± 0.0002
IMCAT	1.272 ± 0.007	-0.0066 ± 0.0005	1.093 ± 0.008	-0.0079 ± 0.0006
ksbm	0.975 ± 0.001	0.0008 ± 0.0001	0.967 ± 0.001	0.0005 ± 0.0001

Table 4. The M, C results for objects SNR > 20 after correcting for selection effects.**Figure 6.** This figure shows the behavior of the shape measurement pipelines as a function of redshift.

function of redshift is shown in Figure 6. The results of bias of the lensing pipelines was quantified by fitting for Q, M and C, and as in 4.1 fitting for only M and C are included in Appendix A for each lensing pipeline.

We find that MJ, DE, PK, I3 and KM show a consistent level of shape measurement bias as a function of redshift. Our results are consistent with an analysis that studied the shape measurement bias as a function of redshift

for im3shape (Kacprzak et al. 2013) on simulated COSMOS galaxies and determined that it did not deviate significantly.

5 STACKED CLUSTER WEAK LENSING

Stacked weak lensing measures the mean tangential shear of background galaxies behind galaxy clusters which are binned by observable parameters such as richness. Since many galaxy clusters are included in the measurement the stacked weak lensing measurement allows for high signal to noise mass measurements on low mass clusters and does not suffer from halo orientation bias, assuming that the galaxy clusters included in each bin are randomly oriented (Weinberg et al. 2012). Stacked weak lensing of clusters in the MaxBCG catalog (Koester et al. 2007; Sheldon et al. 2009) on data from the Sloan Digital Sky Survey (York et al. 2000) has been used to derive cosmological constraints on Ω_m and σ_8 in (Zu et al. 2012; Rozo et al. 2010). Since the DES survey will include deeper imaging and better seeing, the constraints on cosmology from stacked cluster weak lensing should substantially improve.

Although there are a number of systematic effects that can bias the stacked weak lensing measurement including photometric errors, and selection bias of clusters, for the CSTEP project we focus on studying the systematic bias in the stacked weak lensing cluster mass measurement contributed by shape measurement errors. In this paper we

compare the expected statistical errors expected in the DES stacked weak lensing cluster mass measurement which is described in section 5.1 to the bias on the mass from shape measurement errors described in section 5.2.

5.1 Stacked cluster weak lensing: statistical errors

The expected statistical errors on the stacked cluster weak lensing measurement for DES are dominated by the density of sources, and the number of clusters present in each mass and redshift bin. The statistical error we model combines the scatter due to shape noise in background galaxies, and the scatter due to cluster halos not being spherical mass distributions as described in (Weinberg et al. 2012; Becker & Kravtsov 2011). To estimate the number of background galaxies per arcmin² (\overline{ngal}) and their mean redshift for a survey like DES we use a redshift distribution of galaxies

$$f(z) = z^m \exp(-(z/z_*)^\beta) \quad (4)$$

where $m = 2.0$, $z_* = 0.5$ and $\beta = 2.0$ as given in (Weinberg et al. 2012). To determine the number of background sources at a given redshift the background fraction of galaxies is

$$F_{bg} = \frac{\int_0^\infty dz' f(z')}{\int_0^\infty dz' f(z')} \quad (5)$$

which is then used to determine the number of galaxies in sq. arcmin.

$$\overline{ngal} = 10F_{bg}(z) \quad (6)$$

for the DES survey (Rozo, Wu & Schmidt 2011). The average redshift of sources behind the lens for each bin is shown in ?? The statistical error or mass uncertainty $\Delta \ln M$ as described in Weinberg et al. (2012) for stacked weak lensing is :

$$\Delta \ln M = \sqrt{(\Delta \ln M_{shape})^2 + (\sigma_{wl})^2} \quad (7)$$

which combines the error due to the shape noise and the error due to scatter based on clusters not being spherical. From (Becker & Kravtsov 2011) we take

$$\sigma_{wl} = \frac{0.3}{\sqrt{N}} \quad (8)$$

where N is the number of clusters in a given bin. To calculate the shape noise we use the equation

$$\Delta \ln M_{shape} \approx 6.0 * 10^3 \left(\frac{N}{4000} \right)^{1/2} \left(\frac{\sigma_e}{0.3} \right) \left(\frac{M}{2 * 10^{14} M_\odot} \right)^{-2/3} \left(\frac{\overline{ngal}}{30 \text{ arcmin}^{-2}} \right)^{1/2} \left(\frac{D_{ls}/D_s}{0.5} \right)^{-1} \quad (9)$$

from (Weinberg et al. 2012) with $\sigma_e = 0.4$, $\overline{ngal} = 5.72$ and $D_{ls}/D_s = 0.27$ which yields the statistical limits shown in Table ???. To model the concentration we expect for clusters at this redshift we assign an initial concentration c

$$c = A * (m_{200}/(2.0 * 1.e12))^B * (1 + z_{cluster})^C \quad (10)$$

Where $A = 7.85$, $B = -0.081$, $C = -0.71$ and m_{200} is the mass within r_{200} from (?).

5.2 Stacked cluster weak lensing: modeled systematic errors

Here we model the systematic errors on the stacked cluster weak lensing measurement by comparing the average mass

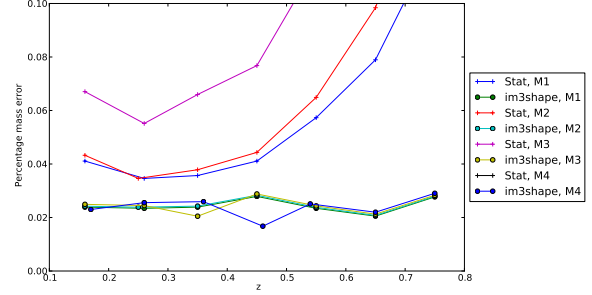


Figure 7. This figure compares the statistical and systematic error of for the stacked weak lensing measurement of the im3shape pipeline on DES.

in each bin to the mass measured by a shear profile, effected by shape measurement bias. To measure the effect of shape measurement bias, a Navarro, Frenk and White (NFW) density profile is created for each mass bin. This density profile is used to calculate the reduced shear g from the theoretical predication as described in Wright & Brainerd (2000).

The NFW density profile is given by

$$\rho(r) = \frac{\delta_c \rho_c}{(r/r_s)(1 + r/r_s)^2} \quad (11)$$

where $\rho_c = \frac{3H^2(z)}{8\pi G}$ is the critical density, $H(z)$ is Hubble's parameter, G is Newton's constant, $r_s = r_{200}/c$, c is the concentration and

$$\delta_c = \frac{200}{3} \frac{c^3}{\ln(1+c) - c/(1+c)} \quad (12)$$

from (Wright & Brainerd 2000). The reduced shear from a NFW halo is

$$g = \frac{\gamma}{1 - \kappa} = \frac{\Delta \Sigma / \Sigma_c}{1 - \overline{\Sigma} / \Sigma_c} \quad (13)$$

The reduced shear as measured by the current measurement pipelines is modeled as

$$g' = g^2 * Q + g * M \quad (14)$$

We then fit this g' distribution to get a M_{200} and c value.

CONCLUSIONS

The CSTEP project determined that

ACKNOWLEDGMENTS

I thank.....

REFERENCES

- Applegate D. E. et al., 2012, ArXiv e-prints
- Becker M. R., Kravtsov A. V., 2011, apj, 740, 25
- Bergé J. et al., 2008, mnras, 385, 695
- Bernstein G. M., 2010, mnras, 406, 2793
- Bertin E., Arnouts S., 1996, aaps, 117, 393

N	Z lens	Z source	Dls/Ds	Mvir	C	M200m	C	M200c	C	$\Delta \ln M$
449	0.16	0.58	0.69	$1.08 \cdot 10^{14}$	5.12	$1.21 \cdot 10^{14}$	5.98	$0.898 \cdot 10^{14}$	4.0	0.044
228	0.16	0.58	0.69	$1.86 \cdot 10^{14}$	4.91	$2.07 \cdot 10^{14}$	5.73	$1.53 \cdot 10^{14}$	3.82	0.046
54	0.16	0.58	0.69	$3.60 \cdot 10^{14}$	4.66	$4.05 \cdot 10^{14}$	5.46	$2.96 \cdot 10^{14}$	3.62	0.068
5	0.17	0.58	0.69	$7.51 \cdot 10^{14}$	4.35	$8.45 \cdot 10^{14}$	5.08	$6.15 \cdot 10^{14}$	3.39	0.173
1079	0.26	0.62	0.54	$1.06 \cdot 10^{14}$	4.85	$1.16 \cdot 10^{14}$	5.5	$0.898 \cdot 10^{14}$	3.89	0.037
528	0.25	0.62	0.54	$1.87 \cdot 10^{14}$	4.63	$2.06 \cdot 10^{14}$	5.26	$1.57 \cdot 10^{14}$	3.71	0.038
109	0.26	0.62	0.54	$3.60 \cdot 10^{14}$	4.39	$3.95 \cdot 10^{14}$	4.97	$3.0 \cdot 10^{14}$	3.51	0.058
10	0.26	0.62	0.54	$6.83 \cdot 10^{14}$	4.17	$7.54 \cdot 10^{14}$	4.73	$5.7 \cdot 10^{14}$	3.33	0.144
1744	0.35	0.66	0.42	$1.05 \cdot 10^{14}$	4.60	$1.13 \cdot 10^{14}$	5.09	$0.902 \cdot 10^{14}$	3.77	0.040
775	0.35	0.66	0.42	$1.83 \cdot 10^{14}$	4.40	$1.98 \cdot 10^{14}$	4.86	$1.57 \cdot 10^{14}$	3.6	0.042
120	0.35	0.66	0.42	$3.64 \cdot 10^{14}$	4.17	$3.94 \cdot 10^{14}$	4.62	$3.1 \cdot 10^{14}$	3.41	0.071
13	0.36	0.66	0.42	$7.30 \cdot 10^{14}$	3.92	$7.92 \cdot 10^{14}$	4.34	$6.19 \cdot 10^{14}$	3.2	0.147
2395	0.45	0.73	0.34	$1.04 \cdot 10^{14}$	4.38	$1.11 \cdot 10^{14}$	4.74	$0.906 \cdot 10^{14}$	3.67	0.046
990	0.45	0.73	0.34	$1.85 \cdot 10^{14}$	4.18	$1.97 \cdot 10^{14}$	4.52	$1.61 \cdot 10^{14}$	3.5	0.049
150	0.45	0.73	0.34	$3.53 \cdot 10^{14}$	3.97	$3.77 \cdot 10^{14}$	4.3	$3.05 \cdot 10^{14}$	3.32	0.084
16	0.46	0.73	0.34	$6.81 \cdot 10^{14}$	3.75	$7.26 \cdot 10^{14}$	4.06	$5.84 \cdot 10^{14}$	3.13	0.173
2753	0.55	0.79	0.26	$1.02 \cdot 10^{14}$	4.19	$1.071 \cdot 10^{14}$	4.44	$0.899 \cdot 10^{14}$	3.56	0.065
985	0.55	0.79	0.26	$1.84 \cdot 10^{14}$	4.00	$1.93 \cdot 10^{14}$	4.25	$1.62 \cdot 10^{14}$	3.4	0.073
138	0.55	0.79	0.26	$3.52 \cdot 10^{14}$	3.80	$3.71 \cdot 10^{14}$	4.04	$3.08 \cdot 10^{14}$	3.23	0.128
13	0.54	0.79	0.26	$6.73 \cdot 10^{14}$	3.61	$7.09 \cdot 10^{14}$	3.85	$5.84 \cdot 10^{14}$	3.06	0.278
3053	0.65	0.87	0.21	$1.01 \cdot 10^{14}$	4.01	$1.05 \cdot 10^{14}$	4.19	$0.89 \cdot 10^{14}$	3.46	0.091
915	0.65	0.87	0.21	$1.82 \cdot 10^{14}$	3.82	$1.89 \cdot 10^{14}$	4.0	$1.61 \cdot 10^{14}$	3.3	0.112
121	0.65	0.87	0.21	$3.52 \cdot 10^{14}$	3.63	$3.66 \cdot 10^{14}$	3.8	$3.11 \cdot 10^{14}$	3.13	0.200
8	0.65	0.87	0.21	$6.97 \cdot 10^{14}$	3.43	$7.25 \cdot 10^{14}$	3.6	$6.13 \cdot 10^{14}$	2.96	0.499
2971	0.75	0.95	0.17	$1.00 \cdot 10^{14}$	3.85	$1.03 \cdot 10^{14}$	3.98	$0.894 \cdot 10^{14}$	3.37	0.142
793	0.75	0.95	0.17	$1.82 \cdot 10^{14}$	3.67	$1.87 \cdot 10^{14}$	3.79	$1.63 \cdot 10^{14}$	3.2	0.184
99	0.75	0.95	0.17	$3.49 \cdot 10^{14}$	3.48	$3.59 \cdot 10^{14}$	3.59	$3.11 \cdot 10^{14}$	3.04	0.338
5	0.75	0.95	0.17	$7.13 \cdot 10^{14}$	3.28	$7.34 \cdot 10^{14}$	3.39	$6.32 \cdot 10^{14}$	2.85	0.942

Table 5. The statistical error or mass uncertainty $\Delta \ln(M)$ as described in Weinberg et al. (2012), for each stacked weak lensing bin modeled for the DES survey.

Bridle S. et al., 2010, *mnras*, 405, 2044
Gillis B. R. et al., 2013, *mnras*, 431, 1439
Heymans C. et al., 2013, *mnras*, 432, 2433
Heymans C. et al., 2006, *mnras*, 368, 1323
Heymans C. et al., 2012, *mnras*, 427, 146
Hildebrandt H. et al., 2012, *mnras*, 421, 2355
Honscheid K., DePoy D. L., 2008, ArXiv e-prints
Kacprzak T., Bridle S., Rowe B., Voigt L., Zuntz J., Hirsch M., MacCrann N., 2013, ArXiv e-prints
Kacprzak T., Zuntz J., Rowe B., Bridle S., Refregier A., Amara A., Voigt L., Hirsch M., 2012, *mnras*, 427, 2711
Kaiser N., Squires G., Broadhurst T., 1995, *apj*, 449, 460
Kilbinger M. et al., 2013, *mnras*, 430, 2200
Kitching T. D. et al., 2012, *mnras*, 423, 3163

Koester B. P. et al., 2007, *apj*, 660, 239
Mahdavi A., Hoekstra H., Babul A., Bildfell C., Jeltrema T., Henry J. P., 2013, *apj*, 767, 116
Massey R. et al., 2007, *mnras*, 376, 13
McBride C., Berlind A., Scoccimarro R., Wechsler R., Busha M., Gardner J., van den Bosch F., 2009, in *Bulletin of the American Astronomical Society*, Vol. 41, American Astronomical Society Meeting Abstracts #213, p. 425.06
Melchior P., Viola M., 2012, *mnras*, 424, 2757
Miller L. et al., 2013, *mnras*, 429, 2858
Mohr J. J. et al., 2008, in *Society of Photo-Optical Instrumentation Engineers (SPIE) Conference Series*, Vol. 7016, Society of Photo-Optical Instrumentation Engineers (SPIE) Conference Series

- Okura Y., Futamase T., 2013, *apj*, 771, 37
Refregier A., Kacprzak T., Amara A., Bridle S., Rowe B.,
2012, *mnras*, 425, 1951
Rozo E. et al., 2010, *apj*, 708, 645
Rozo E., Wu H.-Y., Schmidt F., 2011, *apj*, 735, 118
Schrabback T. et al., 2010, *aap*, 516, A63
Sheldon E. S. et al., 2009, *apj*, 703, 2217
Weinberg D. H., Mortonson M. J., Eisenstein D. J., Hirata
C., Riess A. G., Rozo E., 2012, ArXiv e-prints
Wright C. O., Brainerd T. G., 2000, *apj*, 534, 34
York D. G. et al., 2000, *aj*, 120, 1579
Zu Y., Weinberg D. H., Rozo E., Sheldon E. S., Tinker
J. L., Becker M. R., 2012, ArXiv e-prints
Zuntz J., Kacprzak T., Voigt L., Hirsch M., Rowe B., Bridle
S., 2013, *mnras*, 434, 1604

APPENDIX A: SHEAR MEASUREMENT PIPELINES

A1 im3shape

Im3shape is a model based pipeline.